OPTICA

Observation of canalized phonon polaritons in a single α-MoO$_3$ flake

Kun Wang,[1,†] Zhongao Huang,[1,†] Langlang Xiong,[2,†] Kai Wang,[1,3,*] Yihua Bai,[2] Hua Long,[1] Nan Deng,[1] Bing Wang,[1] Guangwei Hu,[2,5] and Peixiang Lu[1,4,6]

[1]*Wuhan National Laboratory for Optoelectronics and School of Physics, Huazhong University of Science and Technology, Wuhan 430074, China*
[2]*School of Electrical & Electronic Engineering, Nanyang Technological University, 639798, Singapore*
[3]*School of Electronic and Information Engineering, Hubei University of Science and Technology, Xianning 437100, China*
[4]*Hubei Key Laboratory of Optical information and Pattern Recognition, Wuhan Institute of Technology, Wuhan 430205, China*
[5]*guangwei.hu@ntu.edu.sg*
[6]*lupeixiang@hust.edu.cn*
[†]*These authors contributed equally to this work.*
*kale_wong@hust.edu.cn

The canalization effect of phonon polaritons (PhPs) shows highly directional and diffraction-less propagation characteristics in van der Waals (vdW) materials, offering new opportunities to mold the light flow at nanoscale for near-field energy, information, and thermal management. Previously, canalized PhPs have only been experimentally realized in the hexagonal boron nitride metasurface, heterostructures of twisted α-phase molybdenum trioxide (α-MoO$_3$) crystal flakes, or the hybridized system. However, these systems typically have complex structures, and require strict operational conditions, such as fine structural parameters, a specific photonic magic angle, or a doping level of graphene, for realizing polariton canalization with a modest performance. Here, we demonstrate the high-quality PhPs canalization in a single natural α-MoO$_3$ crystal flake. The canalized PhPs exhibit the highly directional and diffraction-free propagation features associated with lateral confinement ratios up to $\lambda_0/80$ (where λ_0 is the free-space wavelength of the incident laser). We believe this work is important to effectively manipulate PhPs in natural vdW materials, with potential applications in nanoimaging, directional energy transfer, and enhanced nonlinearity at the deep subwavelength scale. © 2025

1. INTRODUCTION

Van der Waals (vdW) materials support a full suite of polaritonic responses for emerging nanophotonic applications [1]. One of the prominent polaritonic modes is phonon polaritons (PhPs), which are a hybridization of light and collective atomic lattice vibrations in polar dielectrics [3], facilitating strong light-matter interaction at nanoscale even in the long-wavelength regime [4,5]. Notably, polaritons can exhibit strongly directional electromagnetic energy transport in the predetermined direction, known as the polaritonic canalization mode [6,7]. This happens when the polaritonic iso-frequency contours (IFCs) undergo the topological transition [8,9] from open hyperbolic curves to closed elliptical dispersion lines. The IFCs characterize the propagation direction of polaritonic modes in the momentum space, and they necessarily become flattened during the topological transition. Such polaritonic topological transitions are analogous to Lifshitz transitions in condensed matter physics [10,11], and can showcase anomalous resonant behaviors, such as a dramatic modification of local photonic density of state for enhanced light-matter interactions at the deep subwavelength scale.

The polaritonic canalization modes have been theoretically studied in hyperbolic metamaterials [12] composed of graphene nanoribbons [6,13], and experimentally demonstrated in the nanostructured hexagonal boron nitride metasurface later [7]. However, it typically needs arduous nano-fabrication technology to obtain the anisotropic metasurfaces. Since the anisotropy of the metasurfaces is fundamentally limited by their structural units, the practical performance of these polaritonic phenomena within the metasurfaces is hindered by the auxiliary loss channels, and strong nonlocal effects [14–16]. As a representative vdW polar semiconductor, α-phase molybdenum trioxide (α-MoO$_3$) shows an extreme in-plane anisotropy rooted in its crystal structure, naturally supporting ultra-low-loss anisotropic PhPs [14,17,18]. Recently, the tunable topological transitions and canalization of PhPs were demonstrated in twist-stacked α-MoO$_3$ flakes [19–21]. Furthermore, the canalization of hybridized polaritons has been realized in graphene/α-MoO$_3$ heterostructures by chemically changing the doping level of graphene in the Reststrahlen band (RB) II of α-MoO$_3$ crystals [15,22–25]. However, these reported polaritonic canalization modes require very stringent experimental conditions, such as a specific twist angle or a doping level of

graphene within a narrow frequency range, and complicated heterostructure fabrication procedures. In addition, dynamic tuning of polaritonic modes would meet the demand for the development of further integrated nanophotonic circuits. Thus, the effective manipulation of polaritonic canalization modes with remarkable directionality provides potential applications in various functional flatland optics [26,27], including planar negative reflections [28,29], nanoscale energy transfer [30], and planar hyperlensing [31].

Here, we experimentally demonstrated the wavelength-dependent PhPs canalization with high-quality in a natural α-MoO$_3$ flake through the infrared photo-induced force microscopy (PiFM). This broadband response is ascribed to the two-lobed curve of IFCs with an extreme axial ratio, which is supported by theoretical calculations. The diffraction-free propagation of PhPs canalization mode is further confirmed, and a large confinement ratio up to $\lambda_0/80$ (where λ_0 is the free-space wavelength of the incident laser) is observed. Furthermore, near the optical phonon resonant frequency along the x-axis of the α-MoO$_3$ crystal, resonant materials damping losses caused by the huge imaginary part of the permittivity tensor has a limited influence on the propagation loss of the canalized PhPs, which is rigorously verified by both the analytic calculation and experimental demonstration. Our work provides a feasible approach for tailorable polaritonic canalizations in nanophotonics and polaritonics [32,33].

2. THEORY AND DESIGN

A biaxial vdW material with a low crystalline structural symmetry has multiple RBs ranging from the middle-infrared to far-infrared spectral region [20,34,35], as shown in Figs. 1(a)

and 1(b). Notable, there are additional spectral regimes where theses RBs overlap, resulting in fascinating polaritonic properties. Specifically, the overlapped spectral region between the RB I ($545\,\text{cm}^{-1} \sim 851\,\text{cm}^{-1}$) and RB II ($820\,\text{cm}^{-1} \sim 972\,\text{cm}^{-1}$) refers to two resonance peaks of optical phonons: the transverse optical phonon (TO) along [100] axis (x-axis) at $\omega_{\text{TO}}^x = 820\,\text{cm}^{-1}$, and the longitudinal optical phonon (LO) along [001] axis (y-axis) at $\omega_{\text{LO}}^y = 851\,\text{cm}^{-1}$. Importantly, both real parts of ε_x and ε_y are negative in this peculiar spectral region ($820\,\text{cm}^{-1} \sim 851\,\text{cm}^{-1}$), while $\varepsilon_x/\varepsilon_y$ is calculated up to be several thousands, indicating a remarkably large optical anisotropy. Additionally, the theoretical discovery of canalization effects under resonant conditions has been recently reported [6,36]. Therefore, it is anticipated that there is the possibility of PhPs canalization in a single α-MoO$_3$ flake. Nevertheless, such proximity near the TO along the x-axis (ω_{TO}^x) has a finite influence on the propagation loss of canalized PhPs in the α-MoO$_3$ flake, which we will prove both theoretically and experimentally. So far, the observation of canalized PhPs in a single α-MoO$_3$ flake under this intersected spectral region remains to be addressed, technically due to unavailable continuous-wave excitation light sources for the monochromatic scattering-type scanning near-field optical microscopy (s-SNOM) [20,37], impeding the fundamental understanding and practical exploitation of polariton canalization modes in the single α-MoO$_3$ flake, a natural vdW crystal.

In our experiment, a 160-nm-thick α-MoO$_3$ flake was transferred on the SiO$_2$/Si substrate by an all-dry transfer method (see Section 5). A global Cartesian coordinate is defined in that the x- and y-axes are along the [100] and [001] crystal directions of the α-MoO$_3$ flake, respectively. To characterize the crystalline quality of the α-MoO$_3$ flake, the Raman spectrum was measured to show classical optical phonon resonance frequencies
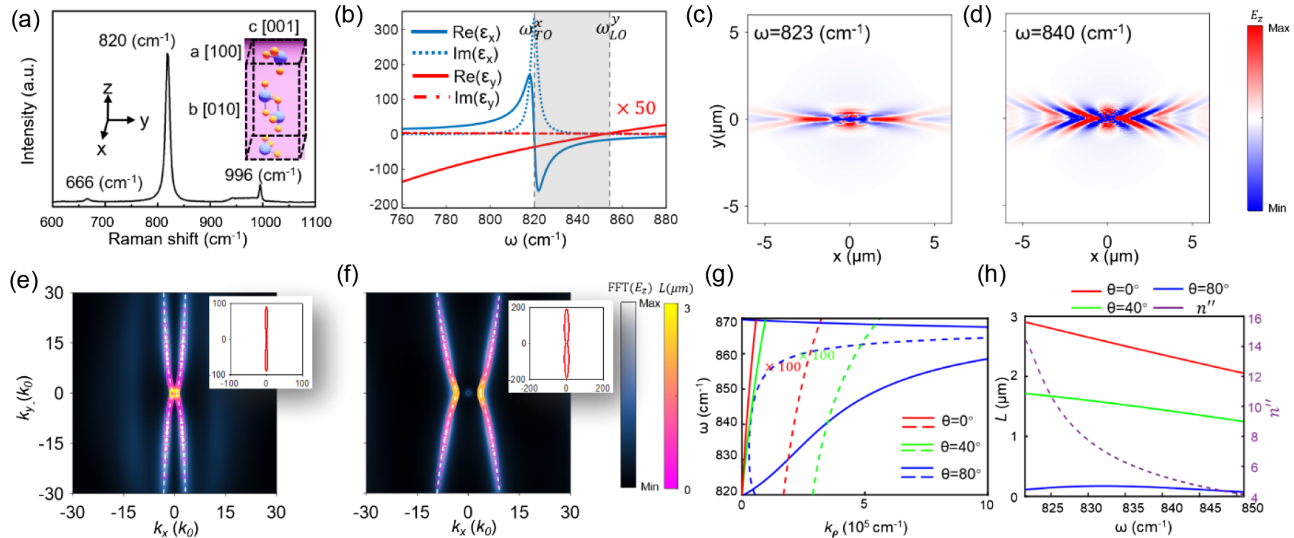

Fig. 1. The canalization effect of phonon polaritons in a single α-MoO$_3$ flake. (a) Raman spectrum of the sample. Black frequency markers indicate the Raman peaks associated with the atomic vibration modes of α-MoO$_3$. The x- and y-axes are along the [100] and [001] crystal directions of α-MoO$_3$, respectively. Inset: schematic of the unit cell of α-MoO$_3$ with three different lattice constants; the molybdenum and oxygen atoms are denoted by the blue and orange spheres, respectively. (b) Real and imaginary parts of the permittivity (ε) along the in-plane principal axes of α-MoO$_3$ with real parts of ε_y multiplied by 50 for clarity. The gray shaded region represents the overlapped spectral region, covering between ω_{TO}^x and ω_{LO}^y. (c), (d) The simulated real-space electromagnetic field (real part of E_z) at the frequency of $820\,\text{cm}^{-1}$ and $840\,\text{cm}^{-1}$, respectively. (e), (f) Numerical dispersions of the frequency at $820\,\text{cm}^{-1}$ (c) and $840\,\text{cm}^{-1}$ (d). The white lines are the analytical dispersion relationships, and the colored circles are the decay length at different wave-vectors. (g) In-plane wave-vectors versus frequencies and azimuth angles $\theta = \text{atan}(\frac{k_y}{k_x})$, where $k_\rho = k_{\rho r} + i k_{\rho i}$, and $k_{\rho r}$ are marked with solid lines, and $k_{\rho i}$ are marked with dashed lines. (h) Length L of $1/e$ power decay away from the bulk α-MoO$_3$ at different directions versus frequencies in the overlapped spectral region between ω_{TO}^x and ω_{LO}^y, and $n'' = \text{Im}(\sqrt{\varepsilon_x})$ is plotted with purple dashed line.

within different RBs of the α-MoO$_3$ crystal [Fig. 1(a)], all indicating excellent crystalline conditions. As shown in Fig. 1(b), the in-plane dielectric permittivities of the α-MoO$_3$ crystal were calculated by multiple Lorentzian oscillator models (see S1 in Supplement 1). The gray shaded region in Fig. 1(b) shows the overlapped spectral region between RB I and RB II in the α-MoO$_3$ crystal (820 cm^{-1} $\sim$ 851 cm^{-1}), where the real parts of ε_x and ε_y are both negative. Particularly, the wave-vector ratio of PhPs along the y-axis (k_y) and x-axis (k_x) is quite large (see S2 in Supplement 1), suggesting the high axial ratio of the corresponding IFCs (thus being close to flat-band) and hence the possibility of highly directional propagation of PhPs, i.e., canalization modes.

To corroborate the above statement, numerical simulations were carried out based on the finite-element method (FEM). A z-oriented dipole was used as the extreme anisotropic PhPs launcher, and the distance between the dipole and the top surface of the α-MoO$_3$ flake was 200 nm. We recorded the z-component of the electric fields (E_z) at a distance of 10 nm above the top surface of the α-MoO$_3$ flake. Figures 1(c) and 1(d) show the simulation results with the frequency (ω_{inc}) of the incident laser at 823 cm^{-1} and 840 cm^{-1}, respectively. As shown in Fig. 1(c), the energy flow of PhPs with ω_{inc} at 823 cm^{-1} is highly collimated along the x-axis, while extremely compressed in the y-axis. As the ω_{inc} is increased to 840 cm^{-1}, the PhPs show hyperbolic-like propagation behaviors. To understand their dispersion features in momentum space, we performed the fast Fourier transform of the Re(E_z) fields and calculated the corresponding analytical dispersion relationships (see S2 in Supplement 1) to extract the corresponding IFCs, which are shown in Figs. 1(e) and 1(f). Surprisingly, both IFCs with ω_{inc} at 823 cm^{-1} and 840 cm^{-1} show an extreme open hyperbolic-like curve, despite that $\varepsilon_x < 0$ and $\varepsilon_y < 0$ in this intersected spectral regime. This is different from the conditions for conventional hyperbolic IFCs in that ε_x and ε_y should be in the opposite sign.

To understand this difference on the open hyperbolic-like IFCs, we calculated the polaritonic dispersion at RB I and RB II of α-MoO$_3$ flake. Specifically, as ω_{inc} increases, the real parts of both k_x and k_y are increased accordingly. Due to the large real part value of k_y ($\sim\lambda_0/30$) at 823 cm^{-1}, the imaginary part of in-plane k (the loss component of PhPs) is great along y-axis, prohibiting its propagation along the above direction. By contrast, k_x is relatively small with ω_{inc} at 840 cm^{-1}, and the propagation loss of PhPs shows a decrease along x-axis since ω_{inc} is far away from the TO phonon resonant frequency along x-axis ($\omega_{\text{TO}}^x = 820$ cm^{-1}). As a result, if we extend the range of the k_x and k_y to a wide momentum range, the corresponding IFCs derived from analytical dispersion relationships will be closed, as shown in the subfigures of Figs. 1(e) and 1(f). However, within the accessible wave-vector range in the near-field experiment for exciting PhPs, the polaritonic dispersion still exhibits open hyperbolic-like curves, which is the major reason of hyperbolic-like PhPs in this spectral region.

Another nonnegligible discussion is on how the imaginary part of the permittivity along x-axis affects the propagation behavior of PhPs, since resonant material damping dominates at the TO phonon resonant frequency. It is widely recognized that materials become lossy near the resonance frequency of the Lorentzian model, but this does not necessarily hold true in our specific polaritonic systems. To clearly demonstrate this, we utilized the analytical dispersion relationships to calculate the in-plane wave-vector $k_\rho = \sqrt{k_x^2 + k_y^2}$ and decay distance (1/e power decay away from the edge of bulk α-MoO$_3$) for various frequencies

and azimuth angles $\theta = \text{atan}(k_y/k_x)$, as shown in Figs. 1(g) and 1(h). The solid and dashed lines in Fig. 1(g) correspond to the real and imaginary parts of k_ρ, respectively. It is observed that despite the concerned frequency range near the resonance frequency at 820 cm^{-1}, the imaginary component of k_ρ of α-MoO$_3$ remains low, leading to a considerable large propagation decay distance, particularly in the x-direction, which also can be found by the colored circles in Figs. 1(e) and 1(f). Furthermore, theoretical analysis indicates that as $|\varepsilon_x|$ approaches infinity, the imaginary component of k_x, which determines the propagation distance at the x-direction, will approach zero, regardless of whether real or imaginary part of ε_x changes (see S2 in Supplement 1 for details).

3. RESULTS AND DISCUSSION

To experimentally verify the striking hyperbolic-like and canalization modes with low loss in the single α-MoO$_3$ flake, we performed the photo-induced force microscopy (PiFM, Molecular Vista) [38–41] for real-space nanoimaging PhPs. The PiFM instrument is based on the atomic force microscopy (AFM). It can simultaneously yield the nanoscale resolved topography, and gradient of the near-field optical force generated at the tip-sample region [Fig. 2(a)]. During the near-field experiment, an oscillating Au-coated tip was illuminated by a pulsed p-polarized infrared laser (quantum cascade laser source from 758 cm^{-1} $\sim$ 1850 cm^{-1}, Block Engineering). The tip acts as an infrared antenna to launch PhPs. Then, PhPs propagate outwards, and are reflected by the sample edge towards the tip, giving rise to the PiFM interference fringes with a spacing distance of $\lambda_p/2$ (where λ_p is the wavelength of PhPs). Figures 2(b) and 2(c) present typical PiFM images of the α-MoO$_3$ flake at $\omega_{\text{inc}} = 780$ cm^{-1} and 880 cm^{-1}, both of which are inside hyperbolic IFCs regions. However, the propagation directions of these PhP modes are different at those frequencies, since the fringes are parallel to the x-direction with ω_{inc} at 780 cm^{-1} [Fig. 2(b)], and to the y-direction at $\omega_{\text{inc}} = 880$ cm^{-1} [Fig. 2(c)]. This is because of different open directions of the PhPs hyperbolic dispersion at different frequencies. In particular, it indicated that the topological transition of PhPs from open hyperbolic curves along the y-direction to that along x-direction was realized by simply sweeping the ω_{inc} over the overlapped spectral region between RB I and RB II. For a quantitative analysis of the anisotropic PhPs propagation, we plotted the PhP dispersions, $\omega(k_i)$ ($i = x, y$), from the measured PiFM images of the same α-MoO$_3$ flake (see Fig. S5 and Fig. S6 in Supplement 1). The periods of fringes in PiFM images were extracted to calculate k_i ($i = x, y$) of PhPs. The experimental results agree well with the theoretical predictions shown as a 2D pseudo colored plot of the complex reflectivity in Fig. 2(d) (see S2 in Supplement 1).

By scanning ω_{inc} from 830 cm^{-1} to 870 cm^{-1}, the wavefront evolution of PhPs can be visualized in the PiFM images (see Supplement 1, S4 for more details.). Figure 3(a) clearly displays hyperbolic PhPs at $\omega_{\text{inc}} = 870$ cm^{-1}. With the exciting frequency sweeping from 870 cm^{-1} to 830 cm^{-1}, the measured PiFM images appear to be the open hyperbolic propagation of the wavefront of PhPs around a nanostructure (marked by a gray semicircle icon). It is actually ascribed to the two-lobed curve of IFCs with an increased axial ratio, which is in a good agreement with the theoretical predictions in Figs. 1(g) and 1(h). Interestingly, at $\omega_{\text{inc}} = 830$ cm^{-1}, the PhPs propagate towards the x-axis, which is highly directional and diffraction-free, manifesting a feature of the PhPs canalization mode. Such experimentally observed evolution
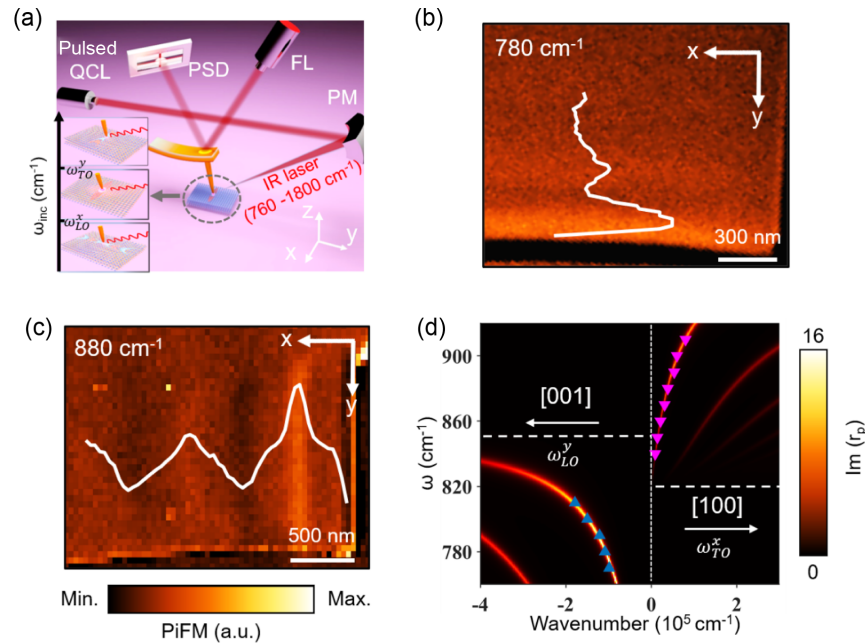
Fig. 2. Photo-induced force nanoimaging of in-plane anisotropic phonon polaritons in the α-MoO$_3$ flake. (a) Schematic of the PiFM microscopy experimental configuration used for nanoimaging of PhPs in α-MoO$_3$. Upon the modulated infrared excitation laser, the metal-coated AFM tip launches the PhPs in the sample. Inset: illustration for wavelength-dependent topological transitions and broadband canalization modes in a crystal α-MoO$_3$ flake. (b), (c) Real-space PiFM images recorded at 780 cm^{-1} and 880 cm^{-1}, respectively. The white line represents the line profile data of the corresponding PiFM images of (b) and (c). Arrows represent the crystal direction of the α-MoO$_3$ flake. (d) Dispersion relations for the PhPs in the α-MoO$_3$ flakes. The pink and blue triangles indicate experimental data corresponding to the PiFM images taken with multiple excitation frequencies along x and y crystal axes of α-MoO$_3$, respectively. The pseudo-colored image represents the calculated imaginary part of the complex reflectivity [Im($r_p(q, w)$)] of the air/α-MoO$_3$/SiO$_2$ multilayered structure.
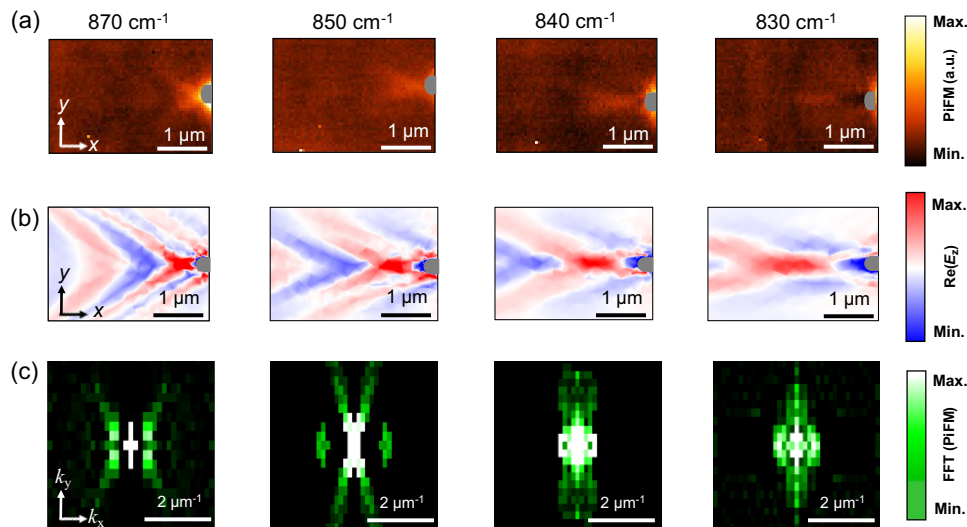

Fig. 3. Tunable topological transitions and broadband PhPs canalization modes in the α-MoO$_3$ sample revealed by PiFM. (a), (b) Real-space near-field images near the apex of a nanorod denoted by the gray semicircle icon, for experimental (a) and the corresponding simulated data (b). Arrows represent the crystal direction of the α-MoO$_3$ flake. (c) Absolute values of the fast Fourier transform of the measured PiFM images in (a). Arrows denote the wavenumber components of PhPs in the momentum space.

of the wavefront of PhPs agrees well with the numerical simulations in Fig. 3(b). Moreover, we extracted the corresponding IFCs in momentum space by performing fast Fourier transform (FFT) of the experimental PiFM images, as plotted in Fig. 3(c). This shows the evolution of the topology of IFCs from the open hyperbola to closed shapes via decreasing ω_{inc} below 851 cm^{-1} (ω_{LO}^y), which is remarkable in a single α-MoO$_3$ flake. To further improve the performance of the canalized PhPs effect, ultra-low-loss PhPs in the α-MoO$_3$ crystal could be realized through the isotope enrichment method [42].

To further demonstrate the diffraction-less propagation nature of PhPs canalization, PiFM measurement was performed around nanohole arrays in the α-MoO$_3$ flake. Figure 4(a) shows the AFM image of nanohole arrays in the α-MoO$_3$ flake. The diameter and
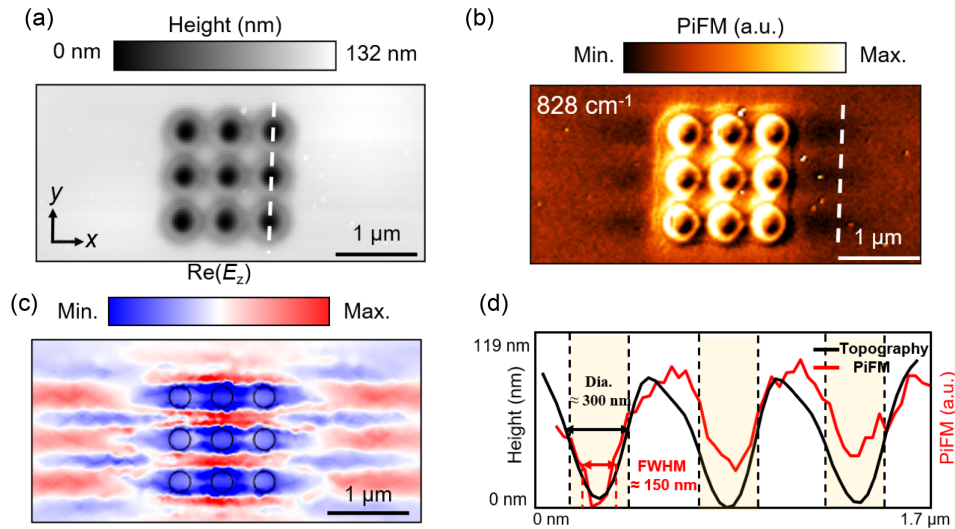
Fig. 4. Diffraction-free propagation of the PhPs canalization mode. (a) Topography of the nanohole arrays. The diameter of each nanohole and the gap between the individual nanoholes are both 300 nm. Arrows represent the crystal direction of the α-MoO$_3$ flake. (b) PiFM images of the nanohole array recorded at 828 cm^{-1}. (c) Simulated Re(E_z) field distributions of the nanohole array. (d) Profiles traced along white dashed line shown in (a) (topography; denoted as the black line) and (b) (PiFM data; marked as the red line), which are separated from each other by 700 nm.

periodicity of nanohole arrays are 300 nm and 600 nm, respectively. At $\omega_{inc} = 828$ cm^{-1}, the measured PiFM image presents the highly directional polaritonic flow along the x-direction as shown in Fig. 4(b). It reveals that the canalized PhPs propagated unidirectionally and were sub-diffractively confined along the y-direction, which is perpendicular to the propagation direction. In Fig. 4(c), it indicates that the numerical simulation of Re(E_z) at the top surface of the nanohole array in the α-MoO$_3$ flake is in good accordance with the experimental data [Fig. 4(b)], featuring the high-performance canalized PhPs modes. To quantitatively analyze the canalized propagation property of PhPs, we extracted profiles of the AFM topography and PiFM image by drawing cutting lines, denoted as white dashed lines in Figs. 4(a) and 4(b), respectively. These two parallel lines are along the y-direction with a separation distance of about 700 nm. In Fig. 4(d), the black and the red lines represent topography data and PiFM amplitude, respectively. Notably, the line profile of topography data shows a gentle boundary [Fig. 4(d)] owing to the topography convolution induced by the nanoscale geometry between the conic AFM tip and the cross-section shape of nanoholes. Nevertheless, the PiFM line profile could exactly reproduce the trend in topography data even at a separation distance of 700 nm. Therefore, it is reasonable to conclude that the canalization angle of PhPs is near zero, and the full-width-at-half-maximum (FWHM) of PhPs canalization modes is estimated around 150 nm, radius of the nanohole, which is $\sim\lambda_0/80$ (where λ_0 is the free-space wavelength). Moreover, the FWHM of PhPs canalization modes may be further reduced if the thickness of the α-MoO$_3$ flake is thinner [43,44].

4. CONCLUSION

In summary, we demonstrated the canalized PhPs supported in a single natural α-MoO$_3$ flake, which serves as a natural platform for realizing the polaritonic canalization. The hyperbolic-like PhPs were surprisingly observed in the intersected spectral region (both $\varepsilon_x < 0$ and $\varepsilon_y < 0$). This is ascribed to the two-lobed curve of IFCs with an extreme axial ratio, which is supported by theoretical

calculations. Furthermore, it is confirmed that PhPs canalization is highly unidirectional and diffraction-free, showing a highly confined ratio of $\lambda_0/80$ along the y-direction. In addition, the PiFM instrument shows the ability of real-space nanoimaging polaritonic modes in vdW materials, providing an alternative tool besides monochromatic s-SNOM to investigate novel polaritonic phenomena at the low-frequency region, especially for ω_{inc} below 880 cm^{-1}. Our work offers a convenient and robust method to effectively manipulate the canalization of PhPs in natural vdW materials and metamaterials [45–47], prompting the potential applications in nanoimaging, subwavelength directional energy transfer, and enhanced nonlinearity at the deep nanoscale [48–50].

5. METHODS

A. Sample Preparations

Bulk crystals of α-MoO$_3$ were purchased from SixCarbon Technology, Shenzhen. Firstly, we mechanically exfoliated the bulk crystals onto a polydimethylsiloxane (PDMS) sheet and inspected the quality of α-MoO$_3$ flakes via an optical microscope (BX 53, Olympus). α-MoO$_3$ flakes with suitable size were then marked and transferred onto a Si/SiO$_2$ (thickness 300 nm) substrate. Focused ion beam lithography (FIB, FEI helios g3) was used to mill the α-MoO$_3$ sample with different defined nanostructures. Note that the milling current was set as low as 8 pA to minimize the implantation of Ga ions, and the milling velocity was around 50 nm per minute for the desired milling depth. After FIB etching, the sample was thermally annealed at 300 °C for 2 h to eliminate the influence of the Ga-ion implantation inside the α-MoO$_3$ flake and could present nearly unchanged polariton propagation.

B. Optical Measurements

PiFM measurements were conducted by means of a commercial Molecular Vista instrument equipped with a pulsed quantum cascade laser (QCL) from Block Engineering. The wavenumber of

the QCL can be tuned between 758 and 1850 cm^{-1}. A metallic-coated AFM tip with the first resonant frequency of ~260 kHz operated in the tapping mode. The second eigenmode of the cantilever was excited for the tip-sample distance stabilization, with a tapping modulation amplitude of a few nanometers and a typical setpoint of 85%. For the PiFM operation, the *p*-polarized QCL was modulated at the frequency difference between the first and second eigenmodes of the AFM cantilever. The photo-induced interaction, i.e., the PiFM signal, was thus mechanically detected at the first eigenmode of the cantilever (see S3 in Supplement 1).

C. Numerical Simulation

The real-space simulation of PhPs in α-MoO$_3$ flakes was performed with the finite-element method (FEM) using COMSOL Multiphysics. For launching highly confined PhPs, a *z*-polarized dipole was placed above the surface of the sample with the distance at 200 nm. The perfectly matched layer was used as the boundary condition for conducting the numerical simulation. We extracted the real part of the *z*-component of the electric field (Re (E_z)) from the top surface of the α-MoO$_3$ flake and its corresponding fast Fourier transform data were then plotted to reveal the iso-frequency dispersion contours of PhPs. The permittivities of the α-MoO$_3$ crystal and the silicon dioxide (SiO$_2$) substrate are discussed in S1 and Table 1 in Supplement 1.

Disclosures. We claim there are no conflicts of interest.

Data availability. Data underlying the results presented in this paper are not publicly available at this time but may be obtained from the authors upon reasonable request.

Supplemental document. See Supplement 1 for supporting content.

REFERENCES

1. D. N. Basov, M. M. Fogler, and F. J. Garcia de Abajo, "Polaritons in van der Waals materials," Science **354**, aag1992 (2016).
2. T. Low, A. Chaves, J. D. Caldwell, *et al.*, "Polaritons in layered two-dimensional materials," Nat. Mater. **16**, 182–194 (2017).
3. G. Ni, A. S. McLeod, Z. Sun, *et al.*, "Long-lived phonon polaritons in hyperbolic materials," Nano Lett. **21**, 5767–5773 (2021).
4. G. Hu, J. Shen, C. W. Qiu, *et al.*, "Phonon polaritons and hyperbolic response in van der Waals materials," Adv. Opt. Mater. **8**, 1901393 (2019).
5. Q. Zhang, G. Hu, W. Ma, *et al.*, "Interface nano-optics with van der Waals polaritons," Nature **597**, 187–195 (2021).
6. J. S. Gomez-Diaz, M. Tymchenko, and A. Alù, "Hyperbolic plasmons and topological transitions over uniaxial metasurfaces," Phys. Rev. Lett. **114**, 233901 (2015).
7. P. Li, G. Hu, I. Dolado, *et al.*, "Collective near-field coupling and nonlocal phenomena in infrared-phononic metasurfaces for nano-light canalization," Nat. Commun. **11**, 3663 (2020).
8. C. Zheng, G. Hu, X. Liu, *et al.*, "Molding broadband dispersion in twisted trilayer hyperbolic polaritonic surfaces," ACS Nano **16**, 13241–13250 (2022).
9. G. Hu, C. Zheng, J. Ni, *et al.*, "Enhanced light-matter interactions at photonic magic-angle topological transitions," Appl. Phys. Lett. **118**, 211101 (2021).
10. I. M. Lifshitz, "Anomalies of electron characteristics of a metal in the high-pressure region," Sov. Phys. JETP **11**, 1130–1135 (1960).
11. H. N. S. Krishnamoorthy, Z. Jacob, E. Narimanov, *et al.*, "Topological transitions in metamaterials," Science **336**, 205–209 (2012).
12. D. Lee, G. Hu, S. So, *et al.*, "Hyperbolic metamaterials: fusing artificial structures to natural 2D materials," eLight **2**, 1–23 (2022).
13. G. Hu, A. Krasnok, Y. Mazor, *et al.*, "Moiré hyperbolic metasurfaces," Nano Lett. **20**, 3217–3224 (2020).
14. W. Ma, P. Alonso-González, S. Li, *et al.*, "In-plane anisotropic and ultra-low-loss polaritons in a natural van der Waals crystal," Nature **562**, 557–562 (2018).
15. H. Hu, N. Chen, H. Teng, *et al.*, "Doping-driven topological polaritons in graphene/α-MoO$_3$ heterostructures," Nat. Nanotechnol. **17**, 940–946 (2022).
16. P. Li, F. J. Alfaro-Mozaz, F. Casanova, *et al.*, "Infrared hyperbolic meta-surface based on nanostructured van der Waals materials," Science **359**, 892–896 (2018).
17. Z. Zheng, J. Chen, Y. Wang, *et al.*, "Highly confined and tunable hyperbolic phonon polaritons in van der Waals semiconducting transition metal oxides," Adv. Mater. **30**, e1705318 (2018).
18. Z. Zheng, N. Xu, S. L. Oscurato, *et al.*, "A mid-infrared biaxial hyperbolic van der Waals crystal," Sci. Adv. **5**, eaav8690 (2019).
19. G. Hu, Q. Qu, G. Si, *et al.*, "Topological polaritons and photonic magic angles in twisted α-MoO$_3$ bilayers," Nature **582**, 209–213 (2020).
20. J. Duan, N. Capote-Robayna, J. Taboada-Gutiérrez, *et al.*, "Twisted nano-optics: manipulating light at the nanoscale with twisted phonon polaritonic slabs," Nano Lett. **20**, 5323–5329 (2020).
21. Z. Zheng, F. Sun, W. Huang, *et al.*, "Phonon polaritons in twisted double-layers of hyperbolic van der Waals crystals," Nano Lett. **20**, 5301–5308 (2020).
22. G. Álvarez-Pérez, A. González-Moran, N. Capote-Robayna, *et al.*, "Active tuning of highly anisotropic phonon polaritons in van der Waals crystal slabs by gated graphene," ACS Photon. **9**, 383–390 (2022).
23. A. Bapat, S. Dixit, Y. Gupta, *et al.*, "Gate tunable light–matter interaction in natural biaxial hyperbolic van der Waals heterostructures," Nanophotonics **11**, 2329–2340 (2022).
24. F. L. Ruta, B. S. Y. Kim, Z. Sun, *et al.*, "Surface plasmons induce topological transition in graphene/α-MoO$_3$ heterostructures," Nat. Commun. **13**, 3719 (2022).
25. Y. Zeng, Q. Qu, L. Liu, *et al.*, "Tailoring topological transitions of anisotropic polaritons by interface engineering in biaxial crystals," Nano Lett. **22**, 4260–4268 (2022).
26. J. S. Gomez-Diaz and A. Alù, "Flatland optics with hyperbolic metasurfaces," ACS Photon. **3**, 2211–2224 (2016).
27. J. Duan, G. Álvarez-Pérez, A. I. F. Tresguerres-Mata, *et al.*, "Planar refraction and lensing of highly confined polaritons in anisotropic media," Nat. Commun. **12**, 4325 (2021).
28. G. Álvarez-Pérez, J. Duan, J. Taboada-Gutiérrez, *et al.*, "Negative reflection of nanoscale-confined polaritons in a low-loss natural medium," Sci. Adv. **8**, eabp8486 (2022).
29. T. Zhang, C. Zheng, Z. N. Chen, *et al.*, "Negative reflection and negative refraction in biaxial van der Waals materials," Nano Lett. **22**, 5607–5614 (2022).
30. R. Deshmukh, S. A. Biehs, E. Khwaja, *et al.*, "Long-range resonant energy transfer using optical topological transitions in metamaterials," ACS Photon. **5**, 2737–2741 (2018).
31. W. Ma, G. Hu, D. Hu, *et al.*, "Ghost hyperbolic surface polaritons in bulk anisotropic crystals," Nature **596**, 362–366 (2021).
32. Q. Zhang, Q. Qu, G. Hu, *et al.*, "Hybridized hyperbolic surface phonon polaritons at α-MoO$_3$ and polar dielectric interfaces," Nano Lett. **21**, 3112–3119 (2021).
33. J. Duan, G. Álvarez-Pérez, K. V. Voronin, *et al.*, "Enabling propagation of anisotropic polaritons along forbidden directions via a topological transition," Sci. Adv. **7**, eabj0127 (2021).
34. W. Dong, R. Qi, T. Liu, *et al.*, "Broad-spectral-range sustainability and controllable excitation of hyperbolic phonon polaritons in α-MoO$_3$," Adv. Mater. **32**, e2002014 (2020).
35. G. Álvarez-Pérez, T. G. Folland, I. Errea, *et al.*, "Infrared permittivity of the biaxial van der Waals semiconductor α-MoO$_3$ from near- and far-field correlative studies," Adv. Mater. **32**, e1908176 (2020).

36. M. He, T. G. Folland, J. Duan, *et al.*, "Anisotropy and modal hybridization in infrared nanophotonics using low-symmetry materials," ACS Photon. **9**, 1078–1095 (2022).

37. Z. Fei, G. O. Andreev, W. Bao, *et al.*, "Infrared nanoscopy of dirac plasmons at the graphene-SiO_2 interface," Nano Lett. **11**, 4701–4705 (2011).

38. J. Liu, S. Park, D. Nowak, *et al.*, "Near-field characterization of graphene plasmons by photo-induced force microscopy," Laser Photon. Rev. **12**, 1800040 (2018).

39. A. Ambrosio, M. Tamagnone, K. Chaudhary, *et al.*, "Selective excitation and imaging of ultraslow phonon polaritons in thin hexagonal boron nitride crystals," Light Sci. Appl. **7**, 27 (2018).

40. M. Poblet, Y. Li, E. Cortes, *et al.*, "Direct detection of optical forces of magnetic nature in dielectric nanoantennas," Nano Lett. **20**, 7627–7634 (2020).

41. M. Tamagnone, A. Ambrosio, K. Chaudhary, *et al.*, "Ultra-confined mid-infrared resonant phonon polaritons in van der Waals nanostructures," Sci. Adv. **4**, eaat7189 (2018).

42. Y. Zhao, J. Chen, M. Xue, *et al.*, "Ultralow-loss phonon polaritons in the isotope-enriched α-MoO_3," Nano Lett. **22**, 10208–10215 (2022).

43. A. Krasnok and A. Alù, "Low-symmetry nanophotonics," ACS Photon. **9**, 2–24 (2022).

44. N. Li, X. Guo, X. Yang, *et al.*, "Direct observation of highly confined phonon polaritons in suspended monolayer hexagonal boron nitride," Nat. Mater. **20**, 43–48 (2021).

45. W. J. Padilla and R. D. Averitt, "Imaging with metamaterials," Nat. Rev. Phys. **4**, 85–100 (2022).

46. R. Yu, R. Alaee, R. W. Boyd, *et al.*, "Ultrafast topological engineering in metamaterials," Phys. Rev. Lett. **125**, 037403 (2020).

47. X. Wang, K. Chang, W. Liu, *et al.*, "Enhanced near-field coupling and tunable topological transitions in hyperbolic van der Waals metasurfaces for optical nanomanipulation," Nanoscale **14**, 7075–7082 (2022).

48. M. Autore, F. J. Alfaro-Mozaz, I. Dolado, *et al.*, "Boron nitride nanoresonators for phonon-enhanced molecular vibrational spectroscopy at the strong coupling limit," Light Sci. Appl. **7**, 17172 (2018).

49. A. Bylinkin, M. Schnell, M. Autore, *et al.*, "Real-space observation of vibrational strong coupling between propagating phonon polaritons and organic molecules," Nat. Photonics **15**, 197–202 (2020).

50. M. Autore, I. Dolado, P. Li, *et al.*, "Enhanced light–matter interaction in 10B monoisotopic boron nitride infrared nanoresonators," Adv. Opt. Mater. **9**, 2001958 (2020).